

The public reporting burden for this collection of information is estimated to average 1 hour per response, including the time for reviewing instructions, searching existing data sources, gathering and maintaining the data needed, and completing and reviewing the collection of information. Send comments regarding this burden estimate or any other aspect of this collection of information, including suggestions for reducing this burden, to Washington Headquarters Services, Directorate for Information Operations and Reports, 1215 Jefferson Davis Highway, Suite 1204, Arlington VA, 22202-4302. Respondents should be aware that notwithstanding any other provision of law, no person shall be subject to any penalty for failing to comply with a collection of information if it does not display a currently valid OMB control number.
PLEASE DO NOT RETURN YOUR FORM TO THE ABOVE ADDRESS.

1. REPORT DATE (DD-MM-YYYY) 21-10-2016	2. REPORT TYPE Final Report	3. DATES COVERED (From - To) 15-Aug-2015 - 14-Aug-2016
---	--------------------------------	---

4. TITLE AND SUBTITLE Final Report: Advanced Optical and Electrical Characterization System for SiGeSn Materials and Devices	5a. CONTRACT NUMBER W911NF-15-1-0365
	5b. GRANT NUMBER
	5c. PROGRAM ELEMENT NUMBER 611103

6. AUTHORS Shui-Qing Yu	5d. PROJECT NUMBER
	5e. TASK NUMBER
	5f. WORK UNIT NUMBER

7. PERFORMING ORGANIZATION NAMES AND ADDRESSES University of Arkansas 210 Administration Building 1 University of Arkansas Fayetteville, AR 72701 -1201	8. PERFORMING ORGANIZATION REPORT NUMBER
---	--

9. SPONSORING/MONITORING AGENCY NAME(S) AND ADDRESS (ES) U.S. Army Research Office P.O. Box 12211 Research Triangle Park, NC 27709-2211	10. SPONSOR/MONITOR'S ACRONYM(S) ARO
	11. SPONSOR/MONITOR'S REPORT NUMBER(S) 66760-EL-RIP.1

12. DISTRIBUTION AVAILABILITY STATEMENT Approved for Public Release; Distribution Unlimited
--

13. SUPPLEMENTARY NOTES The views, opinions and/or findings contained in this report are those of the author(s) and should not be construed as an official Department of the Army position, policy or decision, unless so designated by other documentation.

14. ABSTRACT The requested funds from ARO will be used to build an advanced photoluminescence (PL) and electroluminescence (EL) measurement system to allow for systemic characterizations of GeSn and SiGeSn material and optoelectronic devices. For PL measurement, with the high pumping power, low temperature operation down to 10 K, and long wavelength emission detectability covering 2-5 μm, advanced material optical properties such as carrier lifetime and band alignment could be studied, which provides essential guidance for material growth and device design. The high power continuous wave pumping will provide an easy way to study the GeSn micro disk laser mode behavior.
--

15. SUBJECT TERMS SiGeSn, Optical and Electrical Characterization System

16. SECURITY CLASSIFICATION OF:	17. LIMITATION OF ABSTRACT	15. NUMBER OF PAGES	19a. NAME OF RESPONSIBLE PERSON Shui-Qing (Fisher) Yu
a. REPORT UU	UU		19b. TELEPHONE NUMBER 479-575-7265
b. ABSTRACT UU			
c. THIS PAGE UU			

Report Title

Final Report: Advanced Optical and Electrical Characterization System for SiGeSn Materials and Devices

ABSTRACT

The requested funds from ARO will be used to build an advanced photoluminescence (PL) and electroluminescence (EL) measurement system to allow for systemic characterizations of GeSn and SiGeSn material and optoelectronic devices. For PL measurement, with the high pumping power, low temperature operation down to 10 K, and long wavelength emission detectability covering 2-5 μm , advanced material optical properties such as carrier lifetime and band alignment could be studied, which provides essential guidance for material growth and device design. The high power continuous wave pumping will provide an easy way to study the GeSn micro-disk laser mode behavior. For EL, the objective is to use the system to conduct temperature-dependent study of light-emitting devices, such as light-emitting diodes (LEDs) and laser diodes (LDs) particularly under high injection using the proposed the high power pulsed current source. This will lead to the demonstration of the first electrically injected GeSn based laser. With the new mid-IR detector compatible to both PL and EL measurement, the light detection range will be extended to 3-5 μm range to meet the need of material and device characterization when Sn incorporation into Ge is increased with a bandgap narrower than 0.4 eV. The system will be used to support ongoing DARPA/ARO, AFOSR, and Air Force SBIR projects to develop SiGeSn high performance optoelectronics devices on Si substrates such as emitters and detectors. Other than Group IV photonics, the systems will also serve as a general purpose user facility in PI's group to support other research efforts, for example, the ongoing GaAsBi project and other existing strong III-V material and device research program in UA. In addition to the significant research and technological accomplishments, this project provides graduate and undergraduate training in semiconductor material and device characterizations and development of new infrared materials. The success of this project will undoubtedly lead to opportunities for commercialization of the technical innovations.?

Enter List of papers submitted or published that acknowledge ARO support from the start of the project to the date of this printing. List the papers, including journal references, in the following categories:

(a) Papers published in peer-reviewed journals (N/A for none)

<u>Received</u>	<u>Paper</u>
-----------------	--------------

TOTAL:

Number of Papers published in peer-reviewed journals:

(b) Papers published in non-peer-reviewed journals (N/A for none)

<u>Received</u>	<u>Paper</u>
-----------------	--------------

TOTAL:

Number of Papers published in non peer-reviewed journals:

(c) Presentations

Number of Presentations: 0.00

Non Peer-Reviewed Conference Proceeding publications (other than abstracts):

Received Paper

TOTAL:

Number of Non Peer-Reviewed Conference Proceeding publications (other than abstracts):

Peer-Reviewed Conference Proceeding publications (other than abstracts):

Received Paper

TOTAL:

Number of Peer-Reviewed Conference Proceeding publications (other than abstracts):

(d) Manuscripts

Received Paper

TOTAL:

Number of Manuscripts:

Books

Received Book

TOTAL:

Received

Book Chapter

TOTAL:

Patents Submitted

Patents Awarded

Awards

Graduate Students

<u>NAME</u>	<u>PERCENT SUPPORTED</u>
FTE Equivalent:	
Total Number:	

Names of Post Doctorates

<u>NAME</u>	<u>PERCENT SUPPORTED</u>
FTE Equivalent:	
Total Number:	

Names of Faculty Supported

<u>NAME</u>	<u>PERCENT SUPPORTED</u>
FTE Equivalent:	
Total Number:	

Names of Under Graduate students supported

<u>NAME</u>	<u>PERCENT SUPPORTED</u>
FTE Equivalent:	
Total Number:	

Student Metrics

This section only applies to graduating undergraduates supported by this agreement in this reporting period

The number of undergraduates funded by this agreement who graduated during this period: 0.00

The number of undergraduates funded by this agreement who graduated during this period with a degree in science, mathematics, engineering, or technology fields:..... 0.00

The number of undergraduates funded by your agreement who graduated during this period and will continue to pursue a graduate or Ph.D. degree in science, mathematics, engineering, or technology fields:..... 0.00

Number of graduating undergraduates who achieved a 3.5 GPA to 4.0 (4.0 max scale):..... 0.00

Number of graduating undergraduates funded by a DoD funded Center of Excellence grant for Education, Research and Engineering:..... 0.00

The number of undergraduates funded by your agreement who graduated during this period and intend to work for the Department of Defense 0.00

The number of undergraduates funded by your agreement who graduated during this period and will receive scholarships or fellowships for further studies in science, mathematics, engineering or technology fields:..... 0.00

Names of Personnel receiving masters degrees

NAME
Total Number:

Names of personnel receiving PHDs

NAME
Total Number:

Names of other research staff

NAME PERCENT SUPPORTED
FTE Equivalent:
Total Number:

Sub Contractors (DD882)

Inventions (DD882)

Scientific Progress

See Attachment.

Technology Transfer

N. A.

Advanced Optical and Electrical Characterization System for SiGeSn Materials and Devices

Contract No: W911NF-15-1-0365

Dr. William W. Clark

Report Period: 8/15/2015-8/14/2016

By

Dr. Shui-Qing (Fisher) Yu (PI)

Department of Electrical Engineering

University of Arkansas, Fayetteville, AR

Technical Report

The major achievement during this project was upgrading the following characterization setups in UA:

- I) Photoluminescence measurement setup.
- II) Electroluminescence measurement setup
- III) FTIR setup for detector measurement system

D) Upgrading the photoluminescence measurement setup

Photoluminescence spectroscopy (PL) measurement system has been upgraded by adding two new laser sources, a cryostat for optical pumping measurements and an Indium Antimonide (InSb) detector to detect PL spectra of SiGeSn/GeSn materials up to 5 μm wavelength. The schematic drawing of the PL setup is shown in Fig. 1.

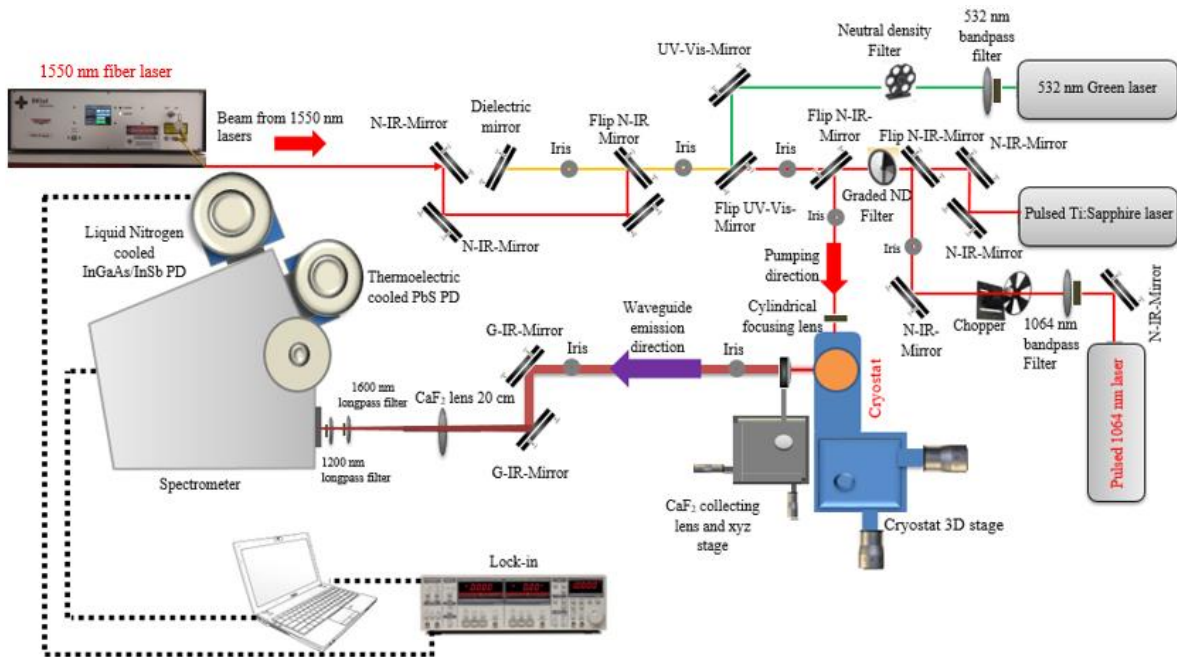


Fig. 1. Photoluminescence spectroscopy measurement setup. The newly added 1064 nm pulsed laser, 1550 nm CW laser, and the cryostat are shown in red.

To upgrade the PL setup, the following key components have been purchased and added to the PL setup:

- A pulsed laser source operating at 1064 nm with repetition rate from 15 to 80 KHz and 14 W maximum power output;
- A continuous wave (CW) fiber laser operating at 1550 nm with 5 W maximum output power;
- A cryostat with a specific sample holder designed for optical pumping measurement;

Here, the functionality of the major components added to the PL setup is explained. The two new laser sources, added to the PL setup, provide a unique capability for excitation of the

SiGeSn/GeSn materials under different excitation energies and pumping powers. i) The high frequency 1064 nm pulsed laser source with repetition rate of 15 to 80 KHz and pulse width of 6 ns and maximum power of 15 W provides a high pumping power for the power-dependent PL measurements and also optical pumping measurements for optically-pumped GeSn laser study. The 1064 nm pulsed laser could provide power densities with a couple of orders of magnitude higher than the previous 532 nm CW laser. It would be beneficial from the physics aspect to use laser sources with higher power and scrutinize the emissions under high power density excitation. The laser power is controlled using the power supply module and further power adjustment is done using an attenuating polarizer. ii) The 1550 nm CW fiber laser with maximum power of 5 W is suitable to study the band minimum excitation of the SiGeSn/GeSn materials with power density of one order of magnitude higher than the one for 532 nm CW laser. iii) The cryostat to conduct optical pumping measurements for the GeSn laser study. Using the new cryostat, a temperature-dependent PL and optical pumping experiments could be done from 4 K to 300 K.

The optical pumping setup was added to the PL setup using a careful modification on the optical design. The new cryostat with four windows was placed on the PL setup for the optical pumping measurements. In general, the pumping excitation laser is focused on the GeSn waveguides from one direction and the lasing spectrum is collected from another direction which is perpendicular to the incident beam. The reason is that the lasing emission emerges from the facet of the waveguides. The optical pumping process includes the excitation of the GeSn waveguides using the 1064 nm pulsed laser. The laser beam was focused to the GeSn waveguide using a cylindrical lens with a focal length of 7.5 mm. The rectangular shape focused beam has a dimension of 3 mm and 20 μm distributed homogeneously on the GeSn waveguide. The emission from the GeSn waveguide was collected with the same CaF_2 collecting lens used in the PL setup. A similar optical path was considered to eventually deliver the GeSn waveguide emission to the spectrometer and detector. Figure 2 shows an image of the PL setup.

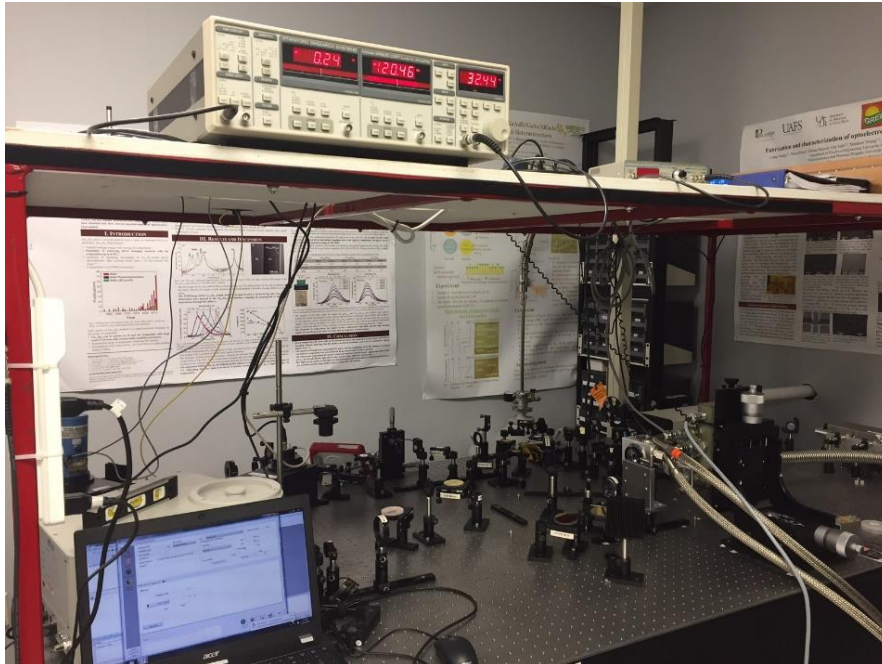


Fig. 2 The PL setup constructed for standard PL and optical pumping measurements.

a) Optical pumping measurement

After upgrading the PL setup and integrating the optical pumping measurement capability to the setup, a series of optical pumping experiments were done on the $\text{Ge}_{0.89}\text{Sn}_{0.11}$ waveguide structures. The $\text{Ge}_{0.89}\text{Sn}_{0.11}$ waveguide was fabricated in clean room using chemical wet etching of the thick $\text{Ge}_{0.89}\text{Sn}_{0.11}$ sample with thickness of 970 nm grown on Ge-buffered Si substrate (100). The material characterization of the thick $\text{Ge}_{0.89}\text{Sn}_{0.11}$ sample is shown in Fig. 3

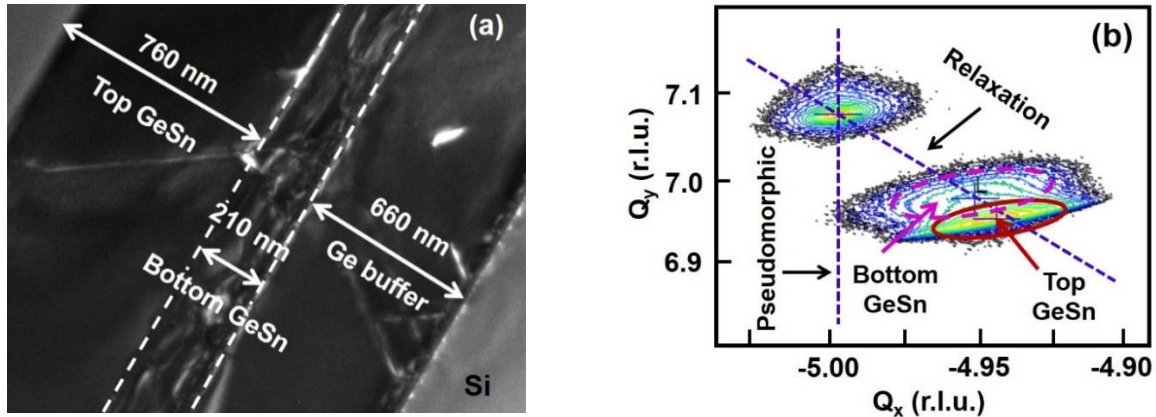


Fig 3. (a) The cross-sectional view TEM image shows two distinct GeSn layers: the bottom layer is defective and with lower Sn composition of 9% while the top layer is almost defect-free and with higher Sn composition of 11%; (b) The RSM contour plot shows the superposition of bottom and top GeSn layers, which are both fully relaxed.

The layer thickness, the Sn composition, and the strain of the sample were carefully analyzed using transmission electron microscopy (TEM) and high-resolution X-ray diffraction (XRD) techniques. Figure 3(a) shows the TEM image of the sample. A 210 nm-thick bottom GeSn layer over the Ge buffer. This layer is defective due to the high density of threading dislocations, which arose mainly from the lattice mismatch between the Ge buffer and the GeSn alloy. The Sn composition in this layer was measured as 9%. A 760 nm-thick high quality top GeSn layer above the bottom GeSn layer. The top GeSn layer achieved extremely high material quality. The reciprocal space map (RSM) of the sample is shown in Fig. 3(b). The broadened contour plot of GeSn indicates the existence of two layers. The part annotated by dashed ellipse corresponds to the bottom GeSn layer, whereas the solid ellipse part featuring full relaxation is associated with the top GeSn layer.

Prior to the waveguide fabrication, the PL spectra of the thick $\text{Ge}_{0.89}\text{Sn}_{0.11}$ sample were measured using the new high frequency 1064 nm pulsed laser. The temperature-dependent and power-dependent PL measurements on the thick $\text{Ge}_{0.89}\text{Sn}_{0.11}$ sample is presented in Fig. 4(a) and 4(b), respectively.

Figure 4(a) shows the temperature-dependent PL spectra under the optical injection level of 270 kW/cm^2 using 1064 nm pulsed laser. Previously, using the 532 nm CW laser, the maximum power density was limited to 15 KW/cm^2 and penetration depth of less than 100 nm in the GeSn sample. The new 1064 nm laser has the penetration depth of almost 1 μm . Note that at the temperature below 100 K, a shoulder at the higher energy side of the main peak was observed (2150 nm). This feature is assigned to the optical transition in GeSn bottom layer (9% Sn) revealed using the 1064 nm pulsed laser. Furthermore, the PL intensity of $\text{Ge}_{0.89}\text{Sn}_{0.11}$ at 10 K could compete with that of the bulk Ge sample, indicating the extremely high material quality.

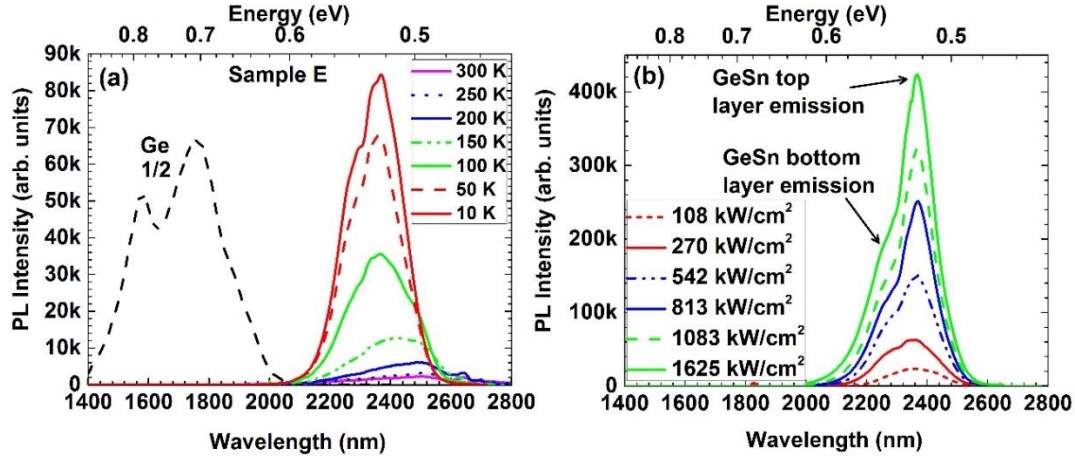


Fig. 4 (a) Temperature-dependent PL spectra of $\text{Ge}_{0.89}\text{Sn}_{0.11}$ using 1064 nm high-frequency laser with 5 ns pulse width at 45 kHz repetition rate as pumping source. The PL of Ge is also plotted for comparison; (b) Pumping power-dependent PL of $\text{Ge}_{0.89}\text{Sn}_{0.11}$ at 10 K. PL emissions from both GeSn top and bottom layers were observed at high optical injection level.

The power-dependent PL measurement at 10 K was conducted to further confirm the transition from GeSn bottom layer, as shown in Fig. 4(b). At low injection level, only a single peak was observed which is associated with the emission from GeSn top layer. As the pumping power exceeds 270 kW/cm^2 , a peak at 2250 nm can be observed, and becomes stronger as the pumping power increases. We thus assigned this peak to the emission from GeSn bottom layer: at relatively low optical injection, almost all photo-generated carriers are confined in a GeSn top layer which features narrower bandgap. As injection level increases, more incident photons were absorbed in GeSn bottom layer, leading to that the radiative recombination could occur in GeSn bottom layer before all the carriers transferred to GeSn top layer. However, the major contribution of PL is always from the optical transitions in GeSn top layer, as can be seen in Fig. 4(b).

The sample was fabricated into a ridge waveguide with 5 μm -width for optical pumping characterization. A low temperature wet chemical etching process was developed in this study. By using the mixture of $\text{HCl}:\text{H}_2\text{O}_2:\text{H}_2\text{O}=1:1:10$ at 0°C , smooth sidewalls were achieved. The average etching rate is $\sim 20 \text{ nm/min}$. The etching depth was measured as 800 nm. Due to the lateral etch, the waveguide width at the top was measured as 3 μm , while at the bottom was measured as 5 μm . The wet etching process developed in this study offers a robust recipe for the fabrication of GeSn-based devices. After etching, the sample was lapped down to $\sim 70 \mu\text{m}$ followed by cleaving to form the mirror-like facets. Devices with cavity lengths of 300, 600, and 1100 μm were investigated in the optical pumping experiment.

Figure 5(a) shows the TEM image of the GeSn waveguide fabricated for the optical pumping experiment. The laser-output versus pumping-laser-input (L-L) curves of the 600 μm -long device at 10 and 90 K is presented in Fig. 5(b) using optical pumping setup. The threshold characteristic was clearly observed. The threshold values were measured as 68 and 166 kW/cm^2 at 10 and 90 K, respectively. The low resolution (1 nm) directional emission spectrum measured at 3 times of the threshold at 90 K is plotted in the Fig. 5 inset (red peak). The FWHM of the peak is 26 nm (5.1 meV). Compared to the FWHM of the PL peak at 10 K (28 meV), the dramatically reduced line-width further confirms the lasing characteristic. The emission spectrum measured at 10 K (not shown) also revealed a similar FWHM of 28 nm (5.6 meV),

which is comparable with that of reported GeSn lasers. The laser operating wavelengths were determined as 2476 and 2503 nm at 10 and 90 K, respectively.

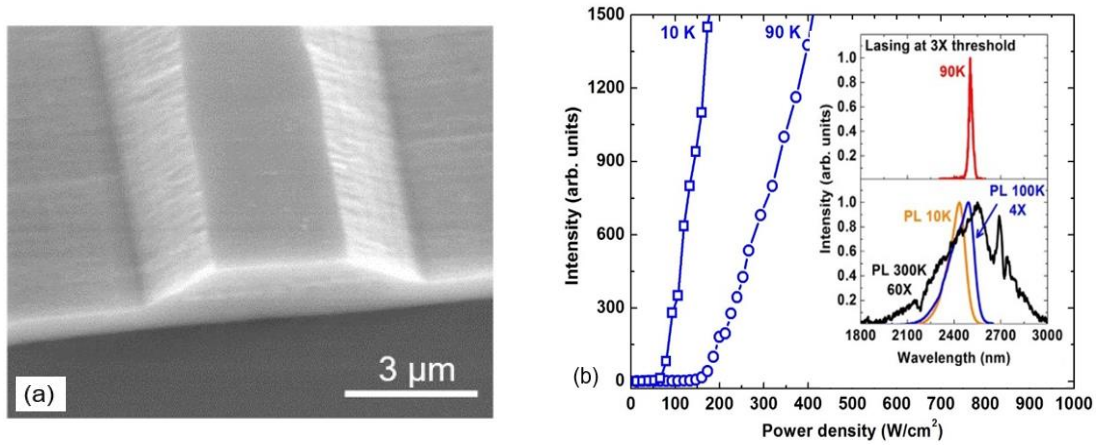


Fig. 5. (a) The SEM image of ridge waveguide device fabricated by wet etching process. (b) The L-L curves of the 600 μm -long edge-emitting device at 10 and 90 K. The thresholds were measured as 68 and 166 kW/cm^2 , respectively. Inset: Optically pumped lasing spectra at 90 K.

To further investigate the lasing mode characteristics, the device with a cavity length of 300 μm was studied. The L-L curve of device at 10 K was plotted in Fig. 6(a) showing a threshold of 106 kW/cm^2 . The high-resolution spectrum (0.1 nm, spectrometer limit) measurement was performed for the device operating at 2 and 5 times of threshold (Fig. 6(a) inset). Due to the relative large area of the cavity facet, the device spectra show a typical multimode lasing characteristic. The spectrum taken under 2 times of threshold shows multi-peaks that are located between 2400 to 2500 nm. As the pumping power increased to 5 times of the threshold, most peaks grow and the overall intensity increases.

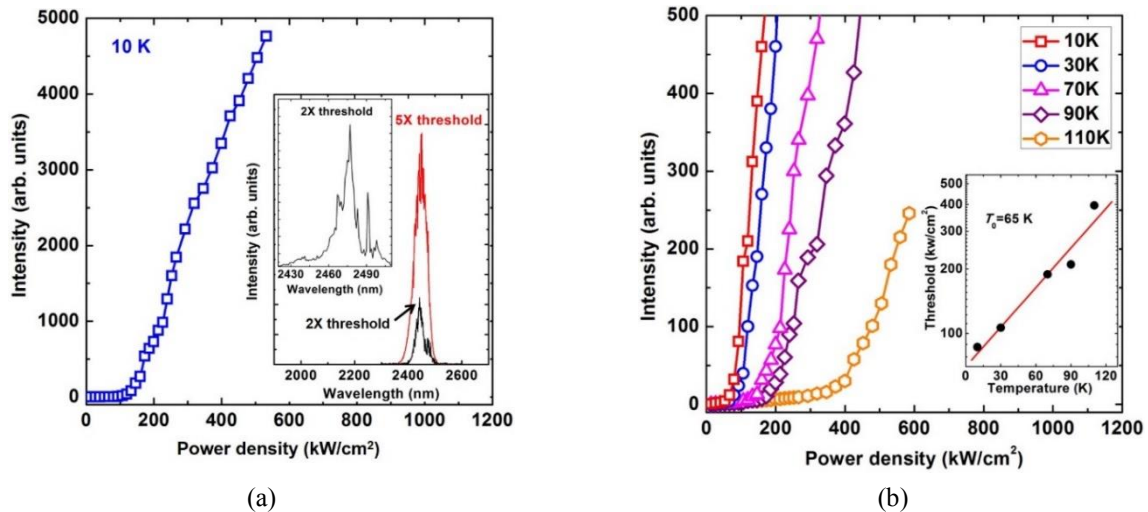


Fig 6. (a) L-L curves of the 300 μm -long edge-emitting device at 10 K. The threshold was measured as 106 kW/cm^2 . Inset: The high resolution spectra under 2 \times and 5 \times threshold pumping power; (b) L-L curves of the 1100 μm -long edge-emitting device taken at the temperatures from 10 to 110 K. The temperature-dependent thresholds were extracted from 87 to 396 kW/cm^2 , based on which the T_0 was extracted as 65 K. Inset: Laser threshold versus temperature for the purpose of fitting T_0 .

The 1100 μm -long device was selected for detailed temperature dependent characteristic study since the longer length cavity reduces the mirror loss and therefore enables the exhibition of the intrinsic characteristics of the material. The L-L curve shows that the lasing operation could reach as high as 110 K, as shown in Fig. 6(b). The measured thresholds range from 87 to 396 kW/cm^2 at the temperatures from 10 to 110 K. The characteristic temperature T_0 was further studied. By fitting the temperature-dependent lasing threshold, the T_0 was extracted as 65 K, as shown in Fig. 6(b) inset. The T_0 was also extracted from L-L curves of 300 and 600 μm -long devices as 78 and 90 K, respectively.

b) Photoluminescence study of SiGeSn/GeSn/SiGeSn quantum wells using different excitation lasers

The SiGeSn/GeSn/SiGeSn QW structures were epitaxially grown on 200 mm Si (100) using an industry standard ASM Epsilon[®] 2000 Plus reduced pressure chemical vapor deposition (RPCVD) system. The low cost commercially available SiH_4 , GeH_4 , and SnCl_4 were used as Si, Ge, and Sn precursors, respectively. A 700-nm-thick Ge buffer layer was grown prior to QW growth by a two-step growth method. The two QW structures with a variation of Si and Sn compositions were grown consisting of a 50-nm-thick SiGeSn barrier, a 10-nm-thick GeSn well, and another 50-nm-thick SiGeSn barrier. A 10-nm-thick Ge cap layer was deposited at the very top. The $\text{Si}_{0.07}\text{Ge}_{0.88}\text{Sn}_{0.05}/\text{Ge}_{0.92}\text{Sn}_{0.08}/\text{Si}_{0.07}\text{Ge}_{0.88}\text{Sn}_{0.05}$ and $\text{Si}_{0.12}\text{Ge}_{0.79}\text{Sn}_{0.09}/\text{Ge}_{0.9}\text{Sn}_{0.1}/\text{Si}_{0.12}\text{Ge}_{0.79}\text{Sn}_{0.09}$ QW structure were labeled as sample A and B, respectively.

The cross-sectional transmission electron microscopy (TEM) and high-resolution X-ray diffraction (HRXRD) was employed to investigate the layer thickness, the Si, and Sn compositions, and the strain for each sample.

Figure 7(a) shows the typical cross-sectional TEM image of sample B. Each layer can be clearly resolved and features low defect density. The high material quality is due to the optimized growth of the Ge buffer which localizes the defects at the Ge/Si interface allowing almost no threading dislocations to propagate to the active layers. The measured thickness of each layer is consistent with the target value within an error of ± 5 nm for the barrier and ± 2 nm for the QW region.

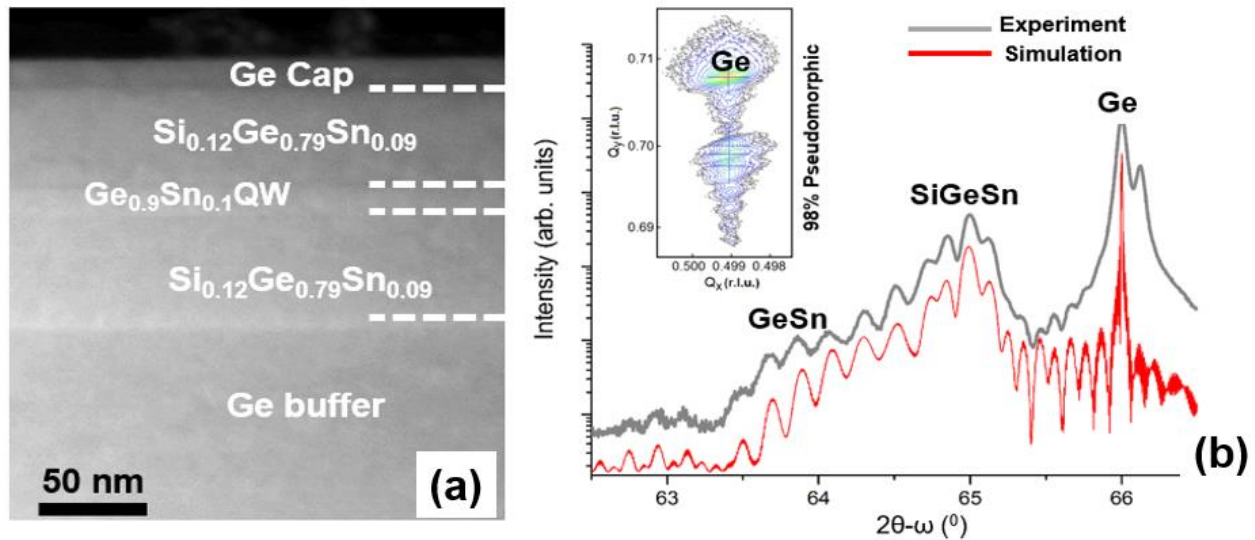


Fig 7. (a) Cross-sectional TEM image of sample B. The XRD 2θ - ω scan of sample B. The gray and red curves are experimental data and simulation results, respectively. Inset: The RSM shows that each layer was grown pseudomorphically to the Ge buffer.

The XRD 2theta-omega ($2\theta/\omega$) scan from (004) plane of sample B is shown in Fig. 7(b). The gray and red curves are plotted according to experimental data and simulation, respectively. The Ge, SiGeSn, and GeSn peaks are clearly observed. The multiple oscillations are associated with the thickness of multi-layered structure (thickness fringes). Their presence indicates the high quality of the interfaces and permits to extract the thickness of the layers. The experimental data agree well with the simulation results. The reciprocal space map (RSM) of sample B performed from asymmetrical plane ($\bar{2}\bar{2}4$) to find the out of plane lattice constant as well as strain information of the layers. The strain calculation of the layers is made based on the slight tensile strain of the Ge buffer layer. The RSM shown in Fig. 7(b) inset reveals that all SiGeSn and GeSn layers are lattice matched (in-plane) to the Ge buffer layer, thus feature compressive strain due to their larger lattice constants compared to that of Ge.

Characterization results achieved through simulation of the XRD results of these two samples are summarized in Table I.

Table I. Information of QW samples in this study

	Sample A				Sample B			
	Si (%)	Sn (%)	Thickness (nm)	Strain (%)	Si (%)	Sn (%)	Thickness (nm)	Strain (%)
Ge cap	0	0	11.0	0.01	0	0	10.0	0.01
SiGeSn barrier	7.00	4.78	50.0	-0.53	12.00	8.51	42.0	-0.84
GeSn well	0	6.97	8.0	-0.80	0	9.51	12.0	-1.59
SiGeSn barrier	7.00	5.61	46.0	-0.41	12.00	9.27	44.5	-0.71
Ge buffer	0	0	700.0	0.01	0	0	700.0	0.01

The photoluminescence of QW structures were studied under different excitation laser sources. The laser sources used in this analysis consist of 1) a 532 nm continuous wave diode-pumped semiconductor laser, 2) a 1064 nm pulsed laser with the pulse width of 5 ns and repetition rate of 45 KHz, and 3) a 1550 nm continuous wave fiber laser. The standard off-axis PL setup was exploited to investigate the PL emission in room temperature and low temperature. Based on the varied power densities and also different penetration depth of the lasers, distinctive PL emission characteristics were observed. Analysis of the PL emission at room temperature and low temperature indicates that the 1064 nm pulsed laser with high power density and large penetration depth increases the carrier concentration in the Ge buffer and cap layers and also SiGeSn layers. That phenomenon suppresses the emission from the GeSn QW region and the PL emission from Ge and SiGeSn would be the dominate emissions while using the 1064 nm pulsed laser. The excitation energy of the lasers and also their penetration depth inside the QW samples are different. The 532 nm laser has higher excitation energy ($E_{exc}=2.33$ eV) than 1064 nm laser ($E_{exc}=1.2$ eV), and both are higher than 1550 nm laser ($E_{exc}=0.8$ eV). Moreover, the penetration depths of the lasers are different in each layer of the QW structure due to the change in the layer absorption coefficients. In order to have a better understanding of the penetration depth of each laser employed in this study, the absorption coefficient of Ge, SiGeSn, and GeSn layers in sample A and B is provided. Simply, $1/(\text{absorption coefficient})$ was considered as a nominal penetration depth for 532 nm, 1064 nm, and 1550 nm wavelength corresponding to the lasers'

wavelengths. As indicated in Table II, the penetration depth of 532 nm laser in the layers of QW structures is less than 50 nm, however, for 1064 nm and 1550 nm lasers, the penetration depths are almost higher than 500 nm stating that both lasers could excite the Ge buffer layer. Thus, the bandgap emission from Ge buffer layer influences on the overall emission of the QW structure.

Table II. The penetration depth of the layers used in the QW structures of sample A and B in 532, 1064, and 1550 nm wavelengths. The units are in nm.

	Sample A			Sample B		
	Ge	Si _{0.07} Ge _{0.88} Sn _{0.05}	Ge _{0.93} Sn _{0.07}	Ge	Si _{0.12} Ge _{0.88} Sn _{0.09}	Ge _{0.9} Sn _{0.1}
532 nm	38	18	20	36	19	21
1064 nm	1006	480	535	1006	503	418
1550 nm	7758	965	1418	7758	780	916

Figure 8 illustrates the excitation energy (a) and estimated penetration depths (b) of 532 nm, 1064 nm, and 1550 nm lasers. As shown in the Figure 8(a), the 532 nm and 1064 nm lasers are able to excite the carriers higher than the Γ valley and L valley minimum of all layers. Lower excitation energy of the 1550 nm laser reduces the carrier densities in the QW structures. On the other hand, both 1064 nm and 1550 nm lasers penetrate all the way down to the Ge buffer layer that eventually enhances the carrier density available for recombination process due to the high thickness of Ge buffer layer. Overall, the 1064 nm laser is able to provide the highest carrier concentration, due to its high penetration depth and also relatively high excitation energy. To investigate the effect of each laser on the optical emission of QW structures, the PL spectra of samples A and B were examined under different excitation lasers using the standard off axis PL setup.

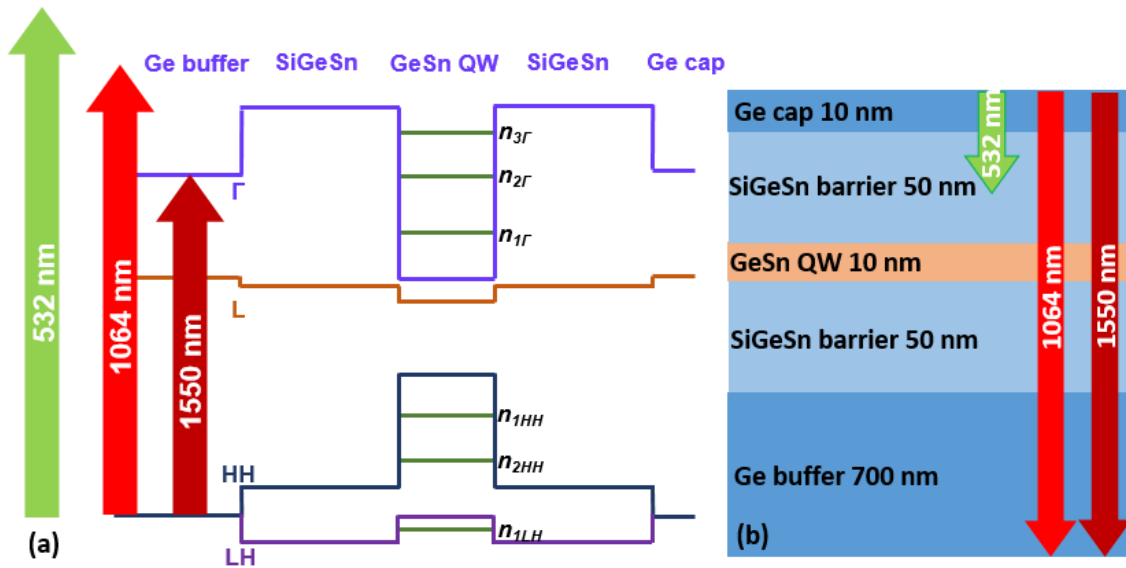


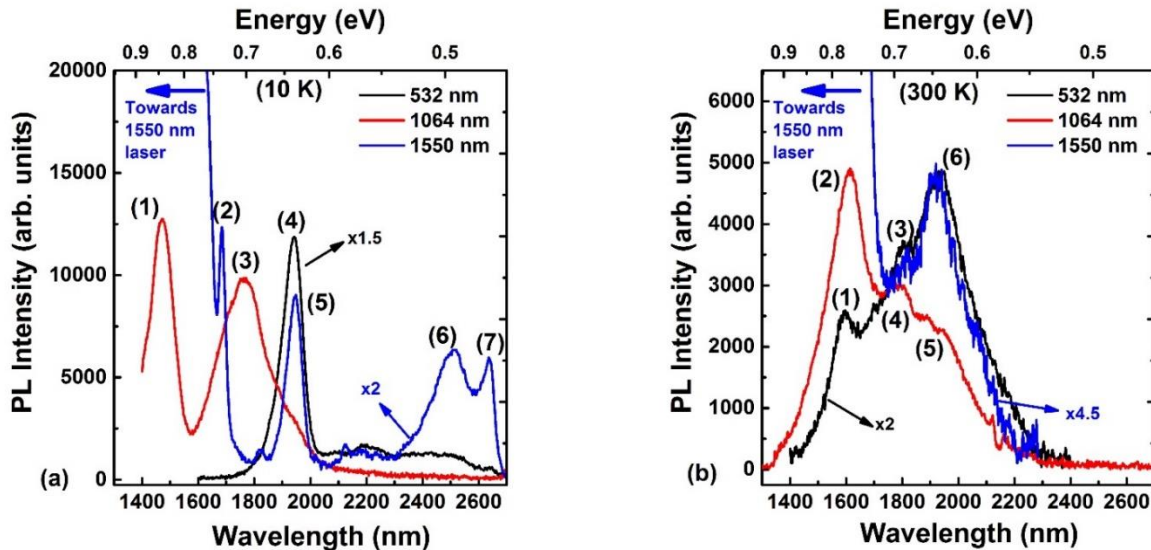
Fig. 8. (a)The illustration of excitation energy of the three lasers used to study the emission of the QW samples. (b) Estimated penetration depth of the three lasers inside the QW structures. None of the diagrams are in scale.

The samples A and B were mounted inside the closed cycle cryostat of the PL setup updated with adding the new excitation lasers. Samples A and B were optically excited using excitation lasers CW 532 nm, pulsed 1064 nm, and CW 1550 nm and the PL spectra of each sample were measured at 10 K and 300 K. The repetition rate of the 1064 nm pulsed laser was 45 KHz and the pulse width was 6 ns. To avoid penetration of the laser sources inside the spectrometer, specific longpass filters were placed in front of the spectrometer entrance slit. The PL emission of sample A and B under different excitation power densities was desired. Therefore, the laser powers were adjusted to different values for that purpose.

Table III. The summarized information of the average power, power densities and the number of incident photons on the samples generated by lasers.

Excitation laser	Average power (W)	Average power density (KW/cm ²)	Peak power density (KW/cm ²)	Energy per pulse (J/cm ²)	Number of incident photons (cm ⁻² s ⁻¹)
532 nm CW	0.65	15	-	-	4×10^{19}
1064 nm pulsed	0.2	-	2.7×10^4	0.13	3×10^{22}
1550 nm CW	0.7	160	-	-	2×10^{21}

As indicated in Table III, the power density of the 1550 nm CW laser was almost one order of magnitude higher than the one for 532 nm CW laser. The peak power density of the pulsed laser was one order of magnitude higher than that of 1550 nm and two orders of magnitude higher than the that of 532 nm laser. Furthermore, the number of incident photons per second per unit area could be calculated for each laser based on their power densities and wavelengths. Calculation of the incident photon numbers could be beneficial to understand the generated carrier density in the QW samples. After adjusting the laser powers based on Table III, the laser beam was delivered to the QW samples and the PL spectra were collected at 10 K and 300 K for sample A and B, respectively. The PL peak positions were extracted to analyze the transitions due to the excitation of carriers. Figure 9(a) and 9(b) show the PL spectra of sample A at 10 K and 300 K, and Figure 9(c) and 8d indicate the PL spectra of sample B at 10 K and 300. The achieved PL spectra from 532 nm, 1064 nm, and 1550 nm lasers are shown in black, red, and blue colors, respectively. All observed peaks in each plot were labeled as numbers in order to clearly identify the peak and describe the related transition.



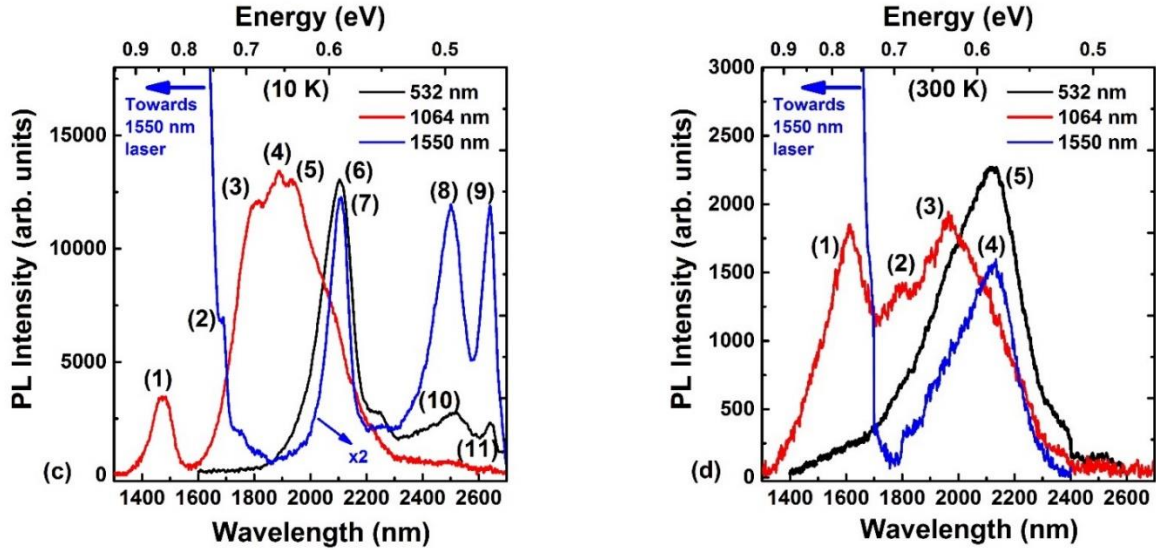


Fig. 9. The PL spectra of sample A at 10 K (a) and 300 K (b) using 532 nm CW laser, 1064 nm pulsed laser and 1550 nm CW laser with different power densities. The PL spectra of sample B at 10 K (c) and 300 K (d) using the same lasers with the same power densities are also presented.

Peaks No. (1) and (2) at 1475 nm and 1688 nm are related to the direct and indirect bandgap transition of Ge buffer layer and cap layer. The transition source of peak No. (3) at 1768 nm is related to the indirect bandgap emission of the SiGeSn barriers. Peaks No. (4) and (5) have almost the same positions at 1947 nm which were attributed to a transition from the first quantized energy level of the L valley ($n1L$) of the conduction band to the first quantized energy level of the heavy-hole ($n1HH$) in the valence band in the GeSn QW. It is important to notice that for the pulsed laser the $n1L$ - $n1HH$ transition in the GeSn QW was not dominant. This phenomenon is related to the high population of the carriers distributed in Ge and SiGeSn layers. High carrier concentrations in the Ge and SiGeSn layers suppress the emission from GeSn QW due to the loss mechanisms. In Fig. 9(a), the PL peak No. (6) and (7) at 2510 nm and 2638 nm are the defect-related emissions. Such an emission from defects has been observed in low temperature PL study of GeSn QWs. Figure 9(b) shows the PL emission of sample A at 300 K. Peak No. (1) and (2) at 1569 nm are related to the direct bandgap transition of Ge buffer layer and cap layer. Peak No. (3) and (4) at 1795 nm are related to the indirect bandgap transition of Ge buffer layer and cap layer. Peak No. (5) and (6) at 1930 nm are related to the first quantized energy level of the Γ valley ($n1\Gamma$) of the conduction band to the $n1HH$ in the valence band. Similar to Fig. 9(a), the PL emission from direct bandgap of Ge is stronger than the PL emission of GeSn QW once the 1064 nm pulsed laser was used. Similarly, it is related to the high carrier density in the Ge and SiGeSn layer that dominates the PL emission. Figure 9(c) represents the PL emission of sample B at 10 K. Similar to Fig. 9(a), the PL peak No. (1) and (2) are related to the direct and indirect PL emission from Ge buffer and cap layers. The PL peaks (3), (4), and (5) are related to the indirect bandgap emission of SiGeSn layers. The reason for multiple PL peaks is related to the variation of thickness and also Si and Sn compositions in the barriers. Peaks (6) and (7) are assigned to the $n1L$ - $n1HH$ indirect transition inside the GeSn QW layer. PL peaks (8) to (11) are attributed to the defect-related emissions at low temperatures. Figure 9(d) depicts the room temperature PL emission spectra from sample B. The peak No. (1) and (2) is related to the

direct and indirect bandgap transition of Ge layers. Peak No. (3) is referred to the indirect bandgap emission of the SiGeSn layers. Thus, using 1064 nm pulsed laser led to no GeSn emission at 300 K for sample B. Peaks No. (4) and (5) are related to the $n1\Gamma-n1HH$ direct transition of GeSn QW.

II) Upgrading the electroluminescence measurement setup

The electroluminescence spectrum measurement setup is constructed for light-emitting diodes (LED) characterization. The system consists of the components of the setup including current/voltage source, multi-mode fiber, optics, temperature control, spectrometer, detector, signal amplifier, and computer. The electrical connection is constructed by connecting the LED device to the current/voltage source by using probe station. A resistor with 50 Ohm resistance is connected in series to ensure the minimum load resistance of the circuits. The emission is collected by the fluorine-based fiber directly coupled from the emission surface of the LED. The collected light is then guided through two CaF_2 lenses and sent to the spectrometer. The pulsed injection is offered by using the pulsed high voltage source newly added to the EL setup. The pulsed current is monitored using inductive current meter. The equipment of the EL setup is fully automatic controlled by using LabVIEW program.

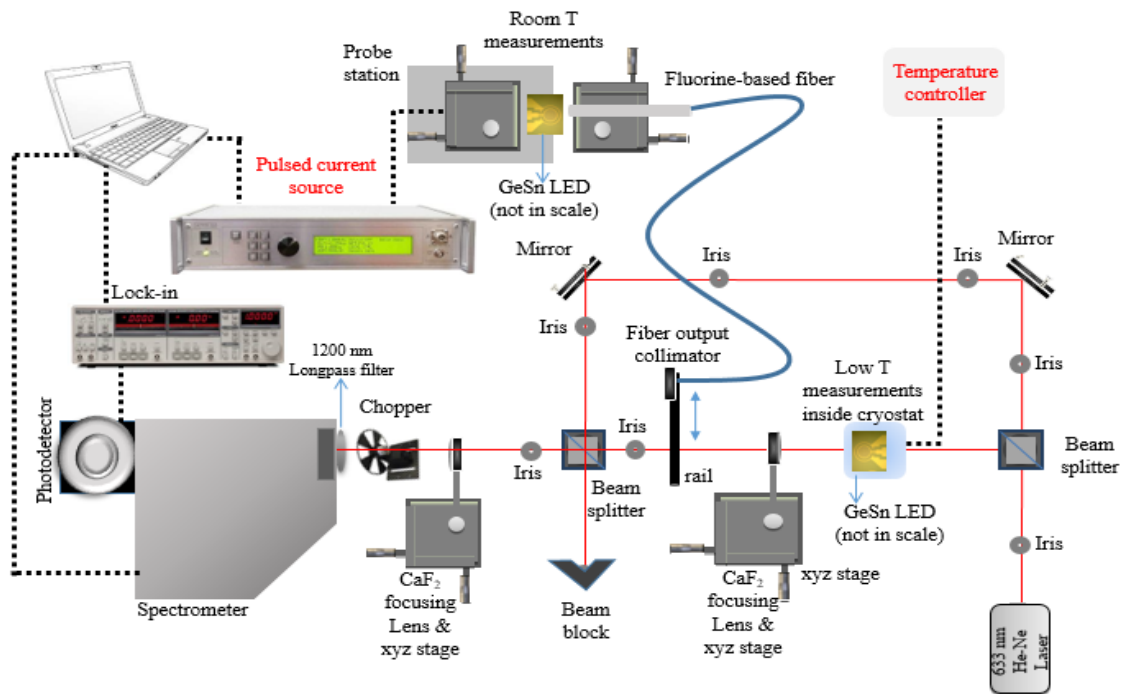


Fig 10. The EL measurement setup with the newly added pulsed current source and temperature controller (in red) for the electrical characterization on the GeSn LEDs in different temperatures.

Each individual equipment communicates with the computer through the GPIB. The typical measurement cycle starts at the turning on of the injection source, followed by the moving the grating position of the spectrometer, and then collected the data from the amplifier voltage reading, where the detector signal is being filtered and amplified; eventually the collected data are plotted and saved. The graphical user interface of the Labview program to synchronize the EL equipment and run the measurements is provided in the following figure.

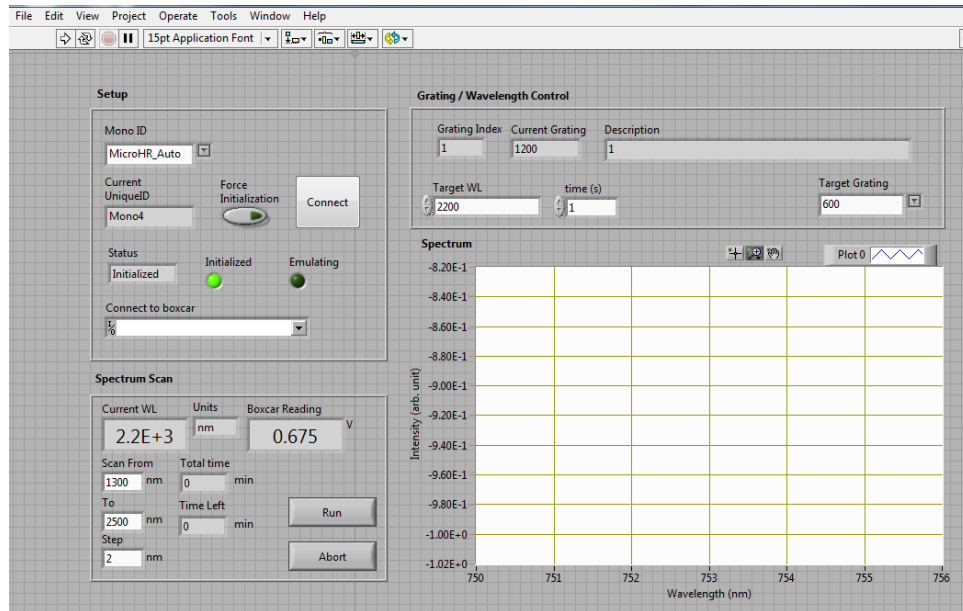


Fig. 11. The Labview program prepared to control the equipment in the EL setup. The pulsed current source, spectrometer and the lock-in amplifier are synchronized to achieve the EL spectrum of the GeSn LEDs.

Due to the relative high noise level of mid-infrared detector comparing to the one for visible range, signal from the detector requires noise suppression to have better signal to noise ratio. Lock-in and boxcar techniques are used for CW and pulse mode injection, respectively. The optical chopper modulates the collected light with a certain frequency, and the lock-in amplifier amplified the signal of that frequency and filtered the noise with the other frequencies. Pulsed signal is amplified using boxcar technique. The pulsed signal is being amplified only during the high level of the pulse. The true signal level is reached by averaging multiple samples of the repeating high levels. Figure 12 shows an image of the EL setup.

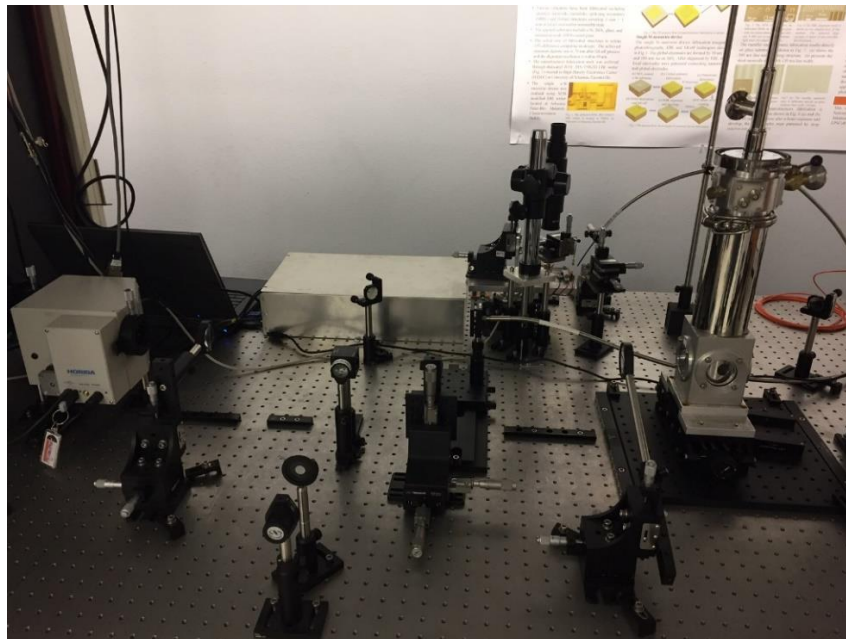


Fig. 12 The EL setup constructed for the electrical characterization of GeSn devices.

The GeSn samples have been fabricated into emitters, including light-emitting diodes (LEDs) and lasers. In-depth characterization of these devices has been conducted. A list of work performed in this year and highlights of results are given in below.

- Temperature-dependent characteristics of GeSn light-emitting diodes with Ge/GeSn/Ge double heterostructure (DHS) and Sn composition up to 10% have been systematically studied. Both photoluminescence and electroluminescence spectra have been characterized at temperatures from 300 to 77 K;
- The electroluminescence emissions under current injection levels from 102 to 357 A/cm² were investigated at 300 K. The monotonic increase of the integrated electroluminescence intensity was observed for each sample;
- The electronic band structures of the DHS were studied. Despite the indirect GeSn bandgap owing to the compressive strain, type-I band alignment was achieved with the barrier heights ranging from 11 to 47 meV;

a) Surface Emitting LED

The samples were fabricated into circular mesa structures with diameters of 100, 250 and 500 μm using photo lithography and etching processes. The LEDs with mesa diameter of 500 μm were selected for EL study since they feature lower dark current density.

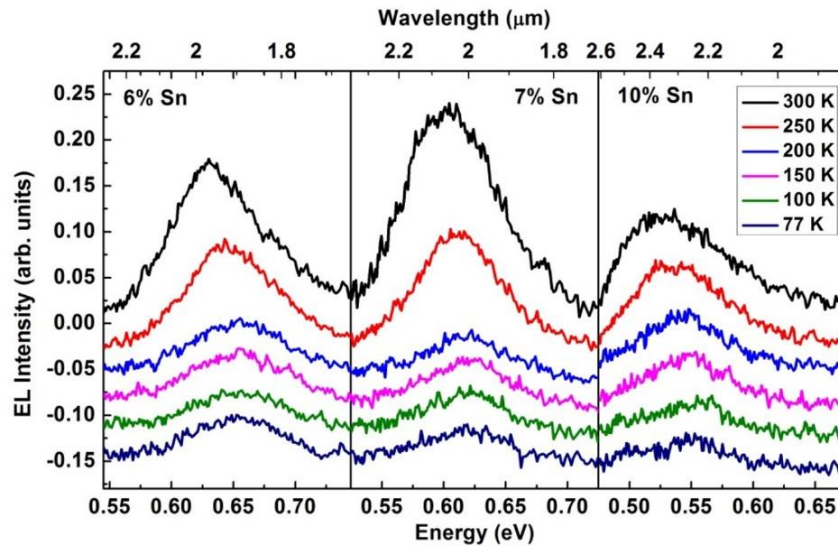


Fig. 13. Electroluminescence spectra of Ge/Ge_{1-x}Sn_x/Ge DHS samples at the temperatures from 300 K to 77 K.

Temperature-dependent EL spectra under an injection current density of 255 A/cm² are shown in Fig. 13. The temperature of the cryostat was controlled using the newly purchased LakeShore temperature controller. For each device, as the temperature decreases from 300 to 77 K, the EL intensity decrease was observed, which agrees with the emission behavior of indirect bandgap material. The main emission peak at each temperature is determined to be the direct band-to-band transition. The position of the main peak blue-shifts as the temperature decreases from 300 to 77 K, which can be explained by the Varshni relation. For the samples with 6, 7 and 10% Sn, the main peak shifts from 0.638 to 0.650 eV, 0.606 to 0.612 eV and 0.537 to 0.546 eV, respectively.

III) Upgrading the FTIR setup for detector measurement

The FTIR detector testing setup has been upgraded by adding two sources inside the FTIR system. The white light source and infrared source have been added to the FTIR, so the detector characterization measurements could be conducted with high performance light sources and provide more accurate photoresponse measurements. The spectral response of GeSn photoconductor which was measured at room temperature using new IR source shows an improvement of 33% in intensity. The enhancement was clearly observed beyond 2 μm .

To further improve the FTIR setup capability, it is necessary to purchase a laser diode beyond 2 μm . At the moment, 2.2 μm laser diode with a power of 3-5mW is sufficient to conduct responsivity measurement of high Sn incorporation photodetector.

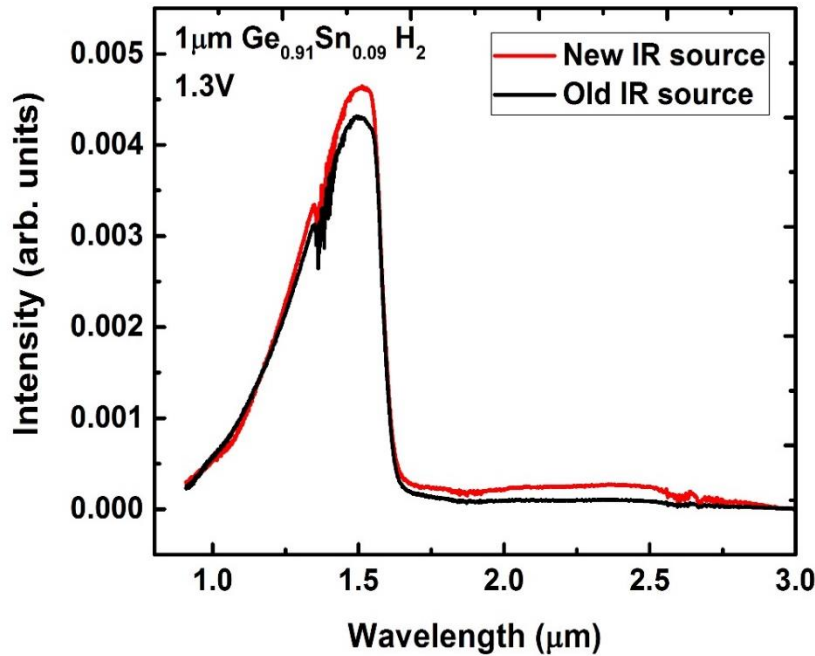


Fig 14. Spectral response of $\text{Ge}_{0.91}\text{Sn}_{0.09}$ photoconductor measured at 1.3V forward bias voltage.

The 9% Sn thick ($\sim 1\mu\text{m}$) GeSn sample was fabricated into photoconductor devices with the fingers width of 3, 6 and 12 μm and corresponding spacing between fingers of 6, 12 and 24 μm , respectively (annotate as 3-6, 6-12 and 12-24 hereafter). Figure 15(a) shows temperature dependent spectral response of 500 μm 3-6 device. The cut-off wavelength of 2.6 μm was observed at 77 K and was extended to longer wavelength as the temperature increases. Compared to our previous study on thin film (less than 200 nm) $\text{Ge}_{0.93}\text{Sn}_{0.07}$ photoconductor, the photo response signal is significantly enhanced, indicating the improved material quality. Moreover, the cut-off wavelength shifts towards longer wavelength. This can be explained as the thicker GeSn layer relaxes the material, which narrows the bandgap of GeSn, resulting in the extended spectral response. Figure 15(b) shows the responsivity of 3-6, 6-12 and 12-24 devices at 77 K, respectively. Since the photoconductive gain is reverse proportional to the carrier transit time, the responsivity increases as the spacing between the electrodes reduces, as shown in Fig. 15(b).

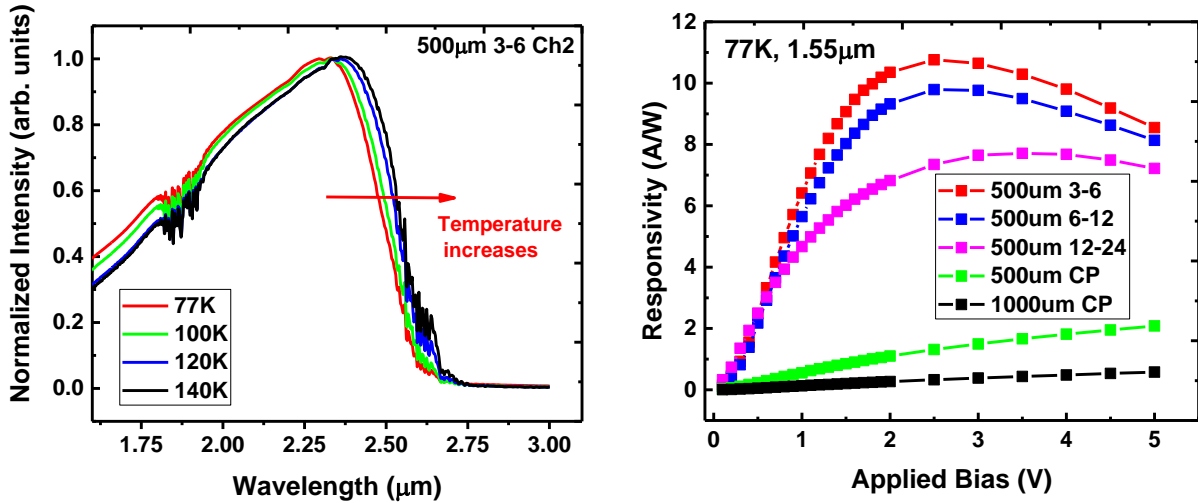


Fig. 15 (a) Temperature dependent spectral response of 500 μm 3-6 photoconductor device. (b) Responsivity at 1.55 μm , 77 K of different devices.

For each device, as the applied bias increases the responsivity increases. The saturation behavior was observed at around 2 V. This behavior in the photoconductive gain is due to the minority carrier sweep-out effect. The temperature dependent responsivity of 3-6 device is plotted in Fig 16. As the temperature decreases, the carrier lifetime increases due to the reduced concentration of scattering centers in the material, therefore more photo generated carriers can be collected before their recombination, resulting in the enhanced photoconductive gain and responsivity.

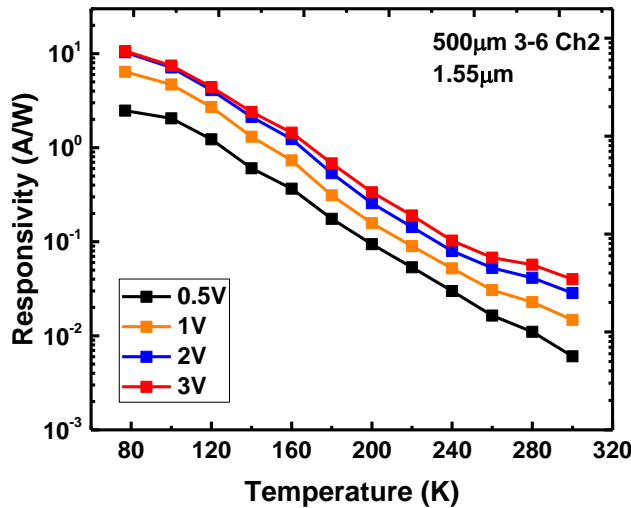


Fig. 16. Temperature dependent responsivity at 1.55 μm of 500 μm 3-6 photoconductor device for different applied voltage.

Spectral D^* of photodiodes (measured at 1 V reverse bias voltage) is shown in Fig. 17 to directly compare with D^* of other market-dominating detectors that use Ge, PbS, InAs, and InGaAs technologies. The spectral response absorption edge is extended to 3 μm at 300 K for the 9% Sn (nominal) photoconductor coplanar device. At 77 K, the cutoff wavelength is 2.6 μm , which is comparable with the response of an extended-InGaAs at 300 K. The peak D^* of 6×10^9

$\text{cm}^*\text{Hz}^{1/2}*\text{W}^{-1}$ was observed at $1.55\ \mu\text{m}$ and $10\ \text{K}$ for interdigitated electrodes photoconductor 3-6 (IEPC). It was later increased to $1.7 \times 10^{10}\ \text{cm}^*\text{Hz}^{1/2}*\text{W}^{-1}$ at $2.35\ \mu\text{m}$ and $10\ \text{K}$. This is on the same order of magnitude and 2-3 times lower than that of extended-InGaAs detectors. The enhancement in D^* is mainly due to thicker GeSn layer. A decrease in the device dark current application of the passivation technique and via reduction of defects layer at the interface of Ge and GeSn would dramatically reduce the noise and therefore significantly improve the D^* of GeSn photodiode detectors, making them competitive with commercially available detector technologies in the above-discussed SWIR FPA applications-space.

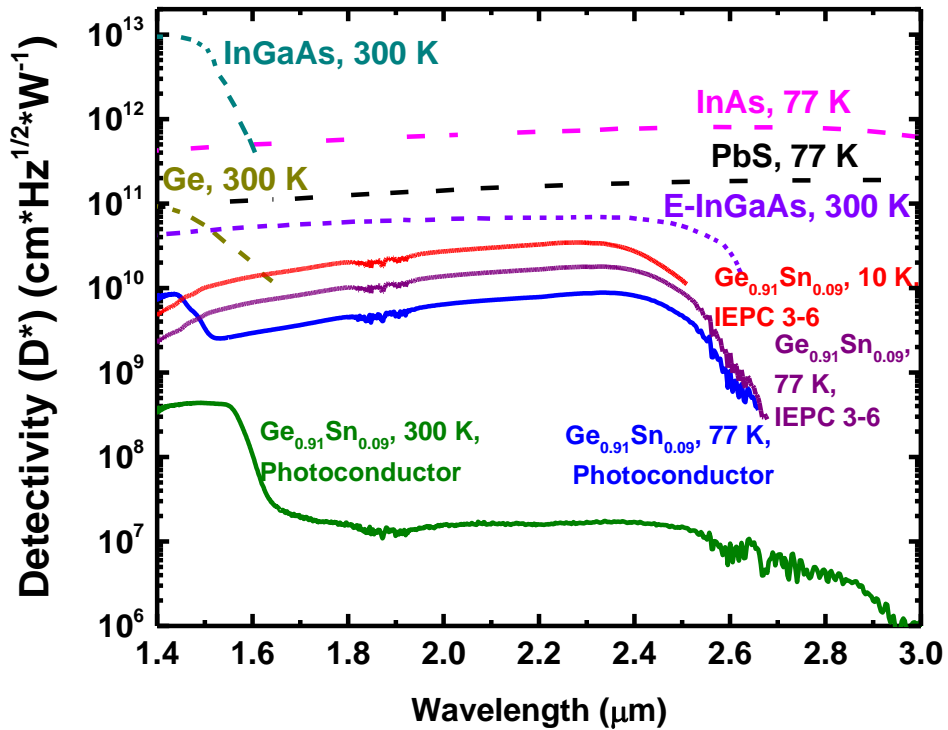


Fig. 17. Spectral D^* of 9% Sn photoconductor measured at 1 V reverse bias voltage across a $500\ \mu\text{m}$ 3-6 device and $500\ \mu\text{m}$ coplanar device. Other market dominating detectors in same spectral range are plotted for comparison.